Title
Spatial and temporal variations of thaw layer thickness and its controlling factors identified using time-lapse electrical resistivity tomography and hydro-thermal modeling

Authors
Tran, Anh Phuong
Dafflon, Baptiste
Bisht, Gautam
et al.

Publication Date
2018-06-01

DOI
10.1016/j.jhydrol.2018.04.028

Peer reviewed

Spatial and Temporal Variations of Thaw Layer Thickness and Its Controlling Factors Identified Using Time-lapse Electrical Resistivity Tomography and Hydro-Thermal Modeling

Anh Phuong Tran, Baptiste Dafflon, Gautam Bisht, Susan S. Hubbard
Earth and Environmental Sciences Area, Lawrence Berkeley National Laboratory

Abstract:

Quantitative understanding of controls on thaw layer thickness (TLT) dynamics in the Arctic peninsula is essential for predictive understanding of permafrost degradation feedbacks to global warming and hydrobiochemical processes. This study jointly interprets electrical resistivity tomography (ERT) measurements and hydro-thermal numerical simulation results to assess spatiotemporal variations of TLT and to determine its controlling factors in Barrow, Alaska. Time-lapse ERT measurements along a 35-m transect were autonomously collected from 2013 to 2015 and inverted to obtain soil electrical resistivity. Based on several probe-based TLT measurements and co-located soil electrical resistivity, we estimated the electrical resistivity thresholds associated with the boundary between the thaw layer and permafrost using a grid search optimization algorithm. Then, we used the obtained thresholds to derive the TLT from all soil electrical resistivity images. The spatiotemporal analysis of the ERT-derived TLT shows that the TLT at high-centered polygons (HCPs) is smaller than that at low-centered polygons (LCPs), and that both thawing and freezing occur earlier at the HCPs compared to the LCPs. In order to provide a physical explanation for dynamics in the thaw layer, we performed 1-D hydro-thermal simulations using the community land model (CLM). Simulation results showed that air temperature and precipitation jointly govern the temporal variations of TLT, while the topsoil organic content (SOC) and polygon morphology are responsible for its spatial variations. When the topsoil SOC and its thickness increase, TLT decreases. Meanwhile, at LCPs, a thicker snow layer and saturated soil contribute to a thicker TLT and extend the time needed for TLT to freeze and thaw. This research highlights the importance of combination of measurements and

numerical modeling to improve our understanding spatiotemporal variations and key controls of TLT in cold regions.

1. Introduction

Thaw layer dynamics and its feedbacks to climate change in permafrost regions are a focus of intensive investigations (e.g., Schuur et al., 2009). Thaw layer dynamics may influence the decomposition of the enormous carbon pool contained in the subsurface, releasing CO_2 and CH_4 to the atmosphere, and therefore, potentially increasing global warming. Thaw layer thickness (TLT) also influences the groundwater direction, surface topography and ecological landscape in the permafrost regions (e.g., Turetsky et al., 2002; Hinzman et al., 2005) as well as the groundwater storage capacity. In turn, the changes in topography and landscape affect the partitioning of precipitation into runoff and infiltration [e.g., Kane et al., 2008]. As a result, it is crucial to quantitatively characterize the thaw layer and its controlling factors to increase our predictive understanding of permafrost system behavior.

Thaw layer dynamics can be explored using numerical simulations or field investigations. Numerical approach considers near-surface atmospheric forcing (e.g., air temperature, precipitation, radiation, wind speed, humidity, and air pressure), vegetation characteristics and soil properties (e.g., porosity, water retention curve, hydraulic conductivity, thermal conductivity, and heat capacity) to simulate the surface-subsurface hydro-thermal processes and thaw layer spatiotemporal variability, often in high resolution. Development of these models is often challenging due to the complexity of hydro-thermal processes that need to be included, such as radiation exchange, evapotranspiration, root water uptake, and snowmelt, as well as water phase transition and its associated landscape deformation (Painter et al., 2013). In addition, the common lack of model input data (e.g., vegetation, soil properties, and bedrock location) and system states (e.g., liquid/ice content, soil temperature, and groundwater table) inhibits calibration and validation of these models.

Combining hydro-thermal modeling with multi-scale observations can lead to improved understanding of the thaw layer dynamics and its drivers. Thaw layer dynamics can be characterized using a range of field-based techniques. Traditional techniques include mechanical probing, vertical soil temperature measurements and visual observations (e.g., Brown et al., 2000). While these traditional techniques provide the relatively accurate measurements of TLT, they are labor – intensive and often do not provide dense spatiotemporal information. Several noninvasive geophysical techniques have demonstrated utility for TLT estimation. For example, Arcone et al. (1998); Hinkel et al. (2001); Jørgensen and Andreasen (2007) and Léger et al. (2017) employed ground-penetrating radar (GPR) to characterize the thaw layer. Schaefer et al. (2015) used Interferometric Synthetic Aperture Radar (InSAR) to estimate the thaw depth at Barrow. You et al. (2013) employed electrical resistivity tomography (ERT), ground temperature monitoring, frost table probing and coring to detect the permafrost depth. Hubbard et al. (2013) combined Lidar data with multiple geophysical (ERT, GPR, electromagnetic) and point measurements to characterize the thaw layer and permafrost variability over a large area. However, the time span of most of these studies were limited, taking place from few measurements to one growing season. There is a lack of data tracking the spatiotemporal variations of TLT over the course of a year, or many years. There have been only few studies that cover several years. For example, Hilbich et al. (2008) used ERT and temperature observations in seven years to explore the long-term and short-term variations of the freezing/thawing process in alpine permafrost and its links to the atmospheric temperature. Dafflon et al. (2017) used one-year multiple datasets obtained from autonomous above- and below-ground measurements, including ERT, to monitor the annual cycle of freezing/thaw dynamics (winter – growing season – freezing) and its link to surface processes.

Besides monitoring TLT, identifying the factors that control TLT dynamics is important as well. Hubbard et al. (2013) found that TLT co-varied with several parameters, including vegetation, soil physical properties, soil water content, polygon morphology and seasonal temperature. Hinzman et al. (1991) and Tran et al. (2017) identified soil organic carbon (SOC) as a main factor that governs the hydro-thermal and thaw layer dynamics in the Alaskan Arctic. Nelson et al. (1998) stated that topography, via near-surface hydrology, is closely linked to the variations of TLT. Wright et al. (2009) reported that the spatial pattern of TLT strongly correlates with the soil moisture distribution, and found that its temporal variations are influenced by air temperature and precipitation. Hinkel and Nelson (2003) analyzed data collected at seven circumpolar active layer monitoring (CALM) sites in northern Alaska during the 1995-2000 period and found that the annual maximum thaw depth is controlled by air temperature. Meanwhile, its spatial variations depend on vegetation, substrate properties, snow cover and soil surface topography. Blok et al. (2010) observed that the shrub expansion in the Arctic region may increase soil temperature and TLT. McClymont et al. (2013) showed that soil temperature in winter in the peat plateau is considerably lower than that in the bog. Dafflon et al. (2017) showed that subsurface soil moisture and thaw depth in the Arctic tundra exhibit a strong correlation with the vegetation greenness. Using numerical simulations, Nicolsky et al. (2007) showed that inclusion of surface SOC in the land surface model could improve the TLT estimation. In a study at Barrow, Alaska, Atchley et al. (2016) performed a sensitivity analysis and found that TLT is the most sensitive to top organic layer thickness and snow depth, but relatively insensitive to water saturation.

The above studies indicate the need to simultaneously investigate the spatiotemporal variations of TLT and identify the factors that control these variations in permafrost regions. Our study addressed this requirement using the following model-data integration approach. We first estimated TLT variations in time and space using time-lapse subsurface electrical resistivity images, which were obtained by inversion of ERT measurements in an ice wedge polygon dominated tundra in Barrow, Alaska. Secondly, we used the probe-based TLT measurements and co-located soil electrical resistivity to determine the electrical resistivity thresholds that separate the thaw layer from the permafrost layer using the grid search optimization algorithm. Then, these thresholds were used to derive TLT from soil electrical resistivity images over a period from 2013 to 2015. Next, we analyzed the annual and multiannual variations of the soil electrical resistivity and TLT. Finally, we performed numerical hydro-thermal simulations to explore TLT dynamics and to investigate the factors that govern these dynamics, including soil properties, morphology and atmospheric forcing. Compared to previous studies, this study advances the knowledge of how to use long-term measurements to provide a more comprehensive picture of the spatiotemporal variability of TLT and its controlling factors. In addition, the joint interpretation of measurements and numerical modeling provides new insights and decreased uncertainty about the controls of TLT dynamics.

2. Description of study site and data availability

Our study site is associated with the Department of Energy's Next-Generation Ecosystem Experiment (NGEE) Arctic project and is situated at the Barrow Environmental Observatory in Alaska (Figure 1). The NGEE site is characterized by ice-wedge polygons, which include low-centered polygon (LCP), flat-centered polygon (FCP) and high-centered polygon (HCP) morphologic features (Hubbard et al., 2013). The polygon morphology largely controls the spatial distribution of snow thickness (Wainwright et al., 2017) and TLT (e.g.,Gangodagamage et al., 2014). In the summer season, while the centers of the LCPs are usually fully filled with water, the HCPs are relatively dry and unsaturated. Sedges, grasses, mosses, and dwarf shrubs are main vegetation types at this site. The mean annual air temperature is around –12°C and that in summer (June to August) is 3.3°C. The annual precipitation is 173 mm in which summer rain contributes up to 42% (Liljedahl et al., 2011). Thawing occurs during the growing season from June to October and the maximum TLT ranges from 25 to 65 cm (Shiklomanov et al., 2010).

We established a 35-m intensive transect at this site, which traverses a HCP, a FCP, and a LCP. An above- and below-ground autonomous measurement system, which included ERT and other measurements, was installed (Figure 1). Probe-based TLT, snow depth, TDR and GPR data were also occasionally manually acquired. Soil samples were collected during the summer of 2014 at the thaw layer of five locations along the transect. In this study, we utilized the time-lapse ERT, probe-based TLT data, and physical soil properties estimated from the soil samples.

The ERT data were acquired along the transect using Wenner-Schlumberger configuration with a 0.5 m electrode spacing. The time-lapse ERT measurements were autonomously acquired daily over a long-time period from 08/15/2013 to 07/07/2016. However, because the last measurements in 2016 were collected at the beginning of the summer season, we only used data from 2013 to 2015 for our spatiotemporal analysis. Details of the acquisition were provided by Dafflon et al (2017).

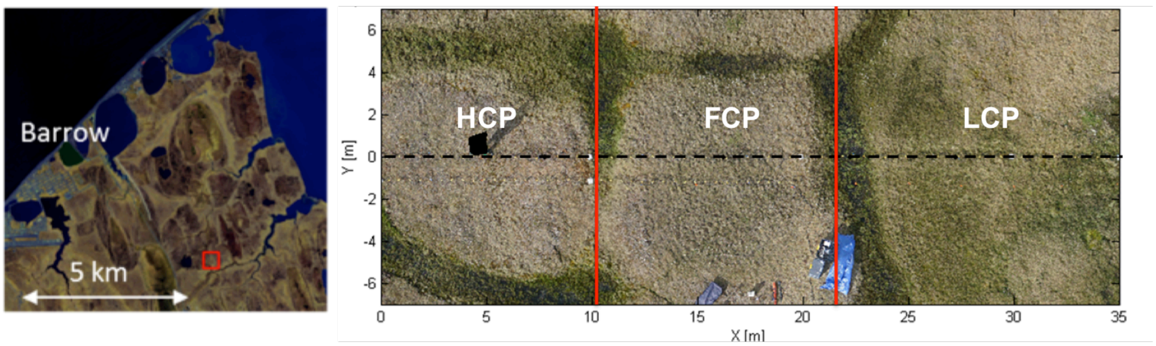

Figure 1: (Left panel) Location of the study site (red square) near Barrow, Alaska, USA. (Right panel) Aerial view of the ERT transect (dashed line), which traverses a high-centered polygon (HCP, $0<X<10$ m), a flat-centered polygon (FCP, $10<X<22$ m) and a low-centered polygon (LCP, $22<X<35$ m). The red lines separate these three polygons.

The time-lapse images of soil electrical resistivity along the transect were obtained by inversion of ERT measurements using the boundless electrical resistivity tomography (BERT) model developed by Rücker et al. (2006). The unstructured mesh was internally generated by BERT and kept the same for all the inversions. The grid cell size, which is controlled by the model, increases from the surface to the bottom layer. In this study, we set the maximum area of a grid cell at 0.5 m^2. The maximum cell width at the surface layer was set at 25% of the electrode spacing (0.5 m). For inversion, we used both electrical resistance and phase data contained in ERT measurements with a relative measurement error of 5%.

The probe-based TLT data were measured at all locations of ERT electrodes (71 locations) on seven days during the 2013 – 2016 period (Figure 2). Based on these measurements and co-located soil electrical resistivity images collected on the nearest days, we estimated the electrical resistivity thresholds that separate the thaw layer and permafrost layer at each electrode location, as described in section 3.2. Then, these thresholds were used to specify TLT from all electrical resistivity images in the period from 08/15/2013 to 12/31/2015.

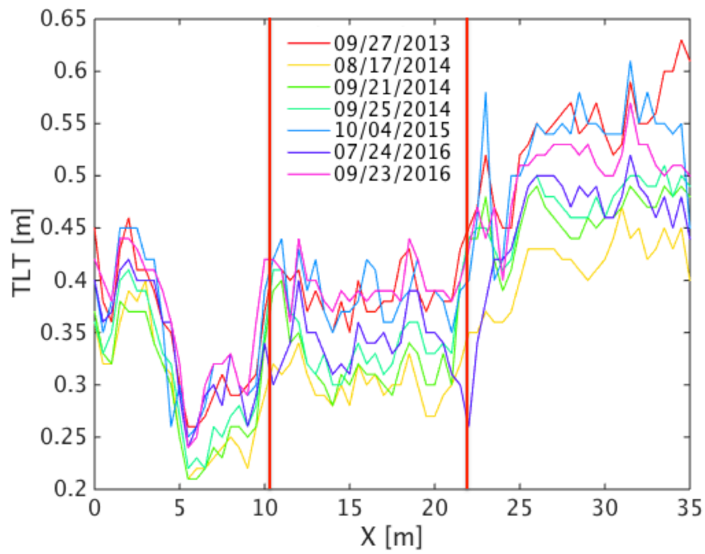

Figure 2: Probe-based TLT data acquired at all ERT electrode locations along the intensive transect during period from 2013 to 2016. Two red solid lines separate the HCP, FCP and LCP.

For evaluating the impact of soil properties on TLT, soil cores of top 0.3 m of the thaw layer were collected at five locations along the ERT transect in summer 2014 using a plastic tube pushed down to various depths and then excavated. In this study, we defined the SOC content as the volumetric fraction of SOC in SOC-mineral mixture without pores as in the Community Land Model (CLM). Table 1 indicates that there is a sharp change in both soil porosity and SOC content between depths of 0.075 and 0.15 m at all locations. For example, at the LCP – SOC location of ~X=29 m (see Figure 1), the porosity reduces from 95% to 82% and the SOC content reduces from 94% to 51%. As for the horizontal variations, the most notable difference in the soil properties is observed at ~X=3 m along the transect and refer later as the HCP – mineral location. Both soil porosity and SOC content at this location are significantly smaller than those at the other locations. For example, the porosity and SOC content of the top 0.075 m at the HCP –

mineral location are respectively 78% and 68%, while at the other locations the porosity is greater than 86% and the SOC content is greater than 94%. Based on various investigations at the NGEE site, the high mineral content at the HCP – mineral location is likely linked to the presence of a type of non-sorted circle that has limited expression at the surface at several locations over the site but mostly in the HCP. There is not much difference in soil properties among the HCP, FCP and LCP. The top 0.075 m at all of the other locations are approximately identical. The spatial variations of soil porosity at depths of 0.15, 0.21 and 0.26 m are significant with the porosity ranging from 51% to 82% and the SOC content ranging from 16% to 51%. It is worth noting that there is another definition of SOC content, which is the percentage of the SOC in total volume of bulk soil (shown at the bottom row of Table 1). Table 1 shows that when the SOC content in soil material increases, the soil porosity increases, and therefore, the SOC content in bulk soil decreases.

Table 1: Soil porosity and volumetric SOC content at depths *z*=0.075, 0.15, 0.21 and 0.26 m and location *X*=3, 8 m (HCP), 12, 17 m (FCP) and 29 m (LCP) along the ERT transect (refer to Figure 1). The SOC content which is defined in CLM as its volumetric percentage in SOC-mineral material was used in this study. For comparison, the SOC content estimated as its volumetric percentage in total volume of bulk soil is also presented.

Polygon type	***HCP***					***FCP***								***LCP***		
***X* (m)**	***3 HCP-mineral location***		***8 HCP-SOC location***			***12 FCP-SOC location***				***17 FCP-SOC location***				***29 LCP-SOC location***		
***z* (m)**	***0.075***	***0.15***	***0.075***	***0.15***	***0.21***	***0.075***	***15***	***0.21***	***0.26***	***0.075***	***0.15***	***0.21***	***0.26***	***0.075***	***0.15***	***0.21***
Porosity (%)	78	38	92	51	66	86	60	68	70	89	63	64	61	95	82	52
SOC (%vol/vol of soil material, CLM)	68	19	96	16	44	95	40	39	46	94	30	31	26	94	51	20
SOC (%vol/vol of bulk soil)	15	12	8	8	15	14	16	13	14	11	11	11	10	5	9	10

3. Spatial and temporal analysis of electrical resistivity and thaw layer thickness

3.1. Spatial and temporal analysis of soil electrical resistivity data

Figure 3 presents the estimated soil electrical resistivity images at specific times over the period from May to November 2014. The figure indicates that vertical variations in electrical resistivity at the end of winter and beginning of summer (05/02/2014 and 06/15/2014), are related to the presence of a shallow frozen active layer and upper permafrost (high resistivity) located over a saline permafrost layer (lower resistivity), the latter documented by Dafflon et al. (2016). During this spring and early summer period, there is not much difference in the vertical resistivity distribution between LCP, FCP, and HCPs. However, when thawing occurs, there is a thaw layer with low resistivity above the permafrost and saline permafrost. We observed that this layer remained relatively conductive until the beginning of winter. In the horizontal direction, Figure 3 shows that TLT at the LCP is larger and remains unfrozen longer than that at the HCP. For example, on 11/16/2016, while there is no thaw layer at the HCP, there is still a shallow thaw layer at the LCP.

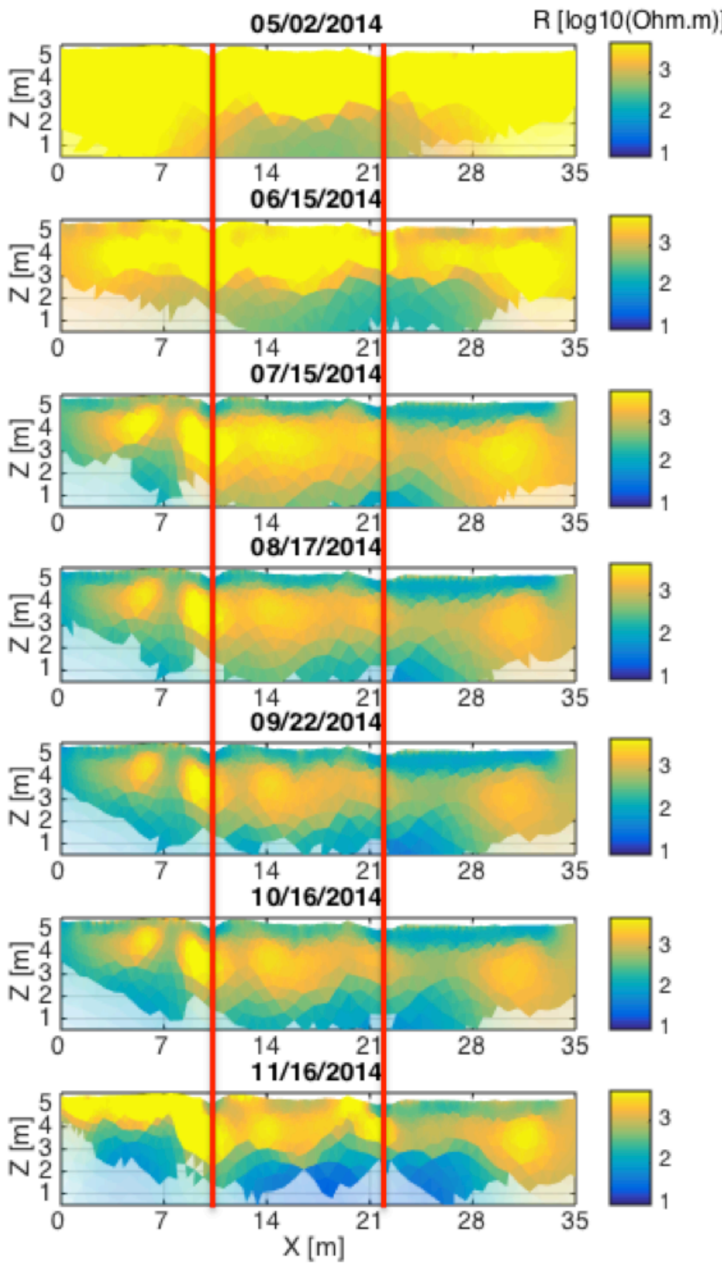

Figure 3: Time-lapse electrical resistivity images (in Log10(Ohm.m)) along the intensive transect. Red lines separate the HCP (left), FCP (middle) and LCP (right). One image per month from May 2014 to November 2014 is shown.

To enable detailed analysis of temporal variations of soil electrical resistivity and its link to soil liquid content in the growing season, we transformed the electrical resistivity to the temporally-normalized value (δ) as below:

$$\delta_{tj} = \frac{\rho_{tj} - \overline{\rho_J}}{\overline{\rho_J}} = \frac{\rho_{tj}}{\overline{\rho_J}} - 1 \tag{1}$$

in which subscripts *t* and *j* denote the measurement at time instant *t* and BERT grid cell *j*; ρ represents the soil electrical resistivity; $\overline{\rho_J} = \frac{1}{M}\sum_{t=1}^{M} \rho_{tj}$ is the temporal mean of electrical resistivity at grid cell *j*; *M* is the number of ERT measurements over the considered period (08/15/2013 – 12/31/2015). The advantage of this normalization is that it removes variability due to soil physical characteristics, which do not change with time, and highlights changes due to freeze state and moisture content. For example, if the relationship between water liquid and soil electrical conductivity follows Archie's formula $\rho = [\phi^m (S_l^n \sigma_w + (\phi^{-m} - 1)\sigma_s)]^{-1}$ (Archie, 1942), the temporally-normalized resistivity at a certain BERT grid cell is formulated as:

$$\delta = \frac{\overline{S_l^n \sigma_w} + (\phi^{-m} - 1)\sigma_s}{S_l^n \sigma_w + (\phi^{-m} - 1)\sigma_s} - 1 \approx \frac{\overline{S_l^n}}{S_l^n} - 1 \tag{2}$$

in which S_l^n is the liquid saturation; $\overline{S_l^n}$ is the temporal mean of S_l^n; ϕ is the soil porosity; σ_w and σ_s are, respectively, the water conductivity and soil surface conductance; and *m* and *n* are the cement and saturation exponential coefficients. Equation (2) illustrates that the temporal normalization removes the effect of temporally constant terms (assuming soil porosity and soil surface conductance do not vary significantly) and highlight the temporal variations of soil liquid water.

The temporal variations of the temporally-normalized resistivity in the 3-month period (August to November) in 2013 and 5-month period (from June to November) in 2014 and 2015 are compared in Figure 4. There were no data in June and July of the year 2013. In general, the soil depth with low resistivity gradually increases from June to reach a maximum in September or October. Compared to 2014, thawing in 2015 occurs earlier. For example, while most of the normalized resistivity on 06/15/2014 is lower than zero at the HCP, thawing occurs at almost the whole transect on 06/15/2015. In addition, of the three years, the normalized resistivity from June to October is lowest in 2014. However, the lowest normalized resistivity in November is observed in 2013. These results imply that the air temperature in the summer of 2015 was highest, but coldest in the winter (see Figure 9), while the winter of 2013 is warmest. This fact will be clarified in the later section where numerical simulations are performed to physically explain the spatiotemporal variations of soil electrical resistivity.

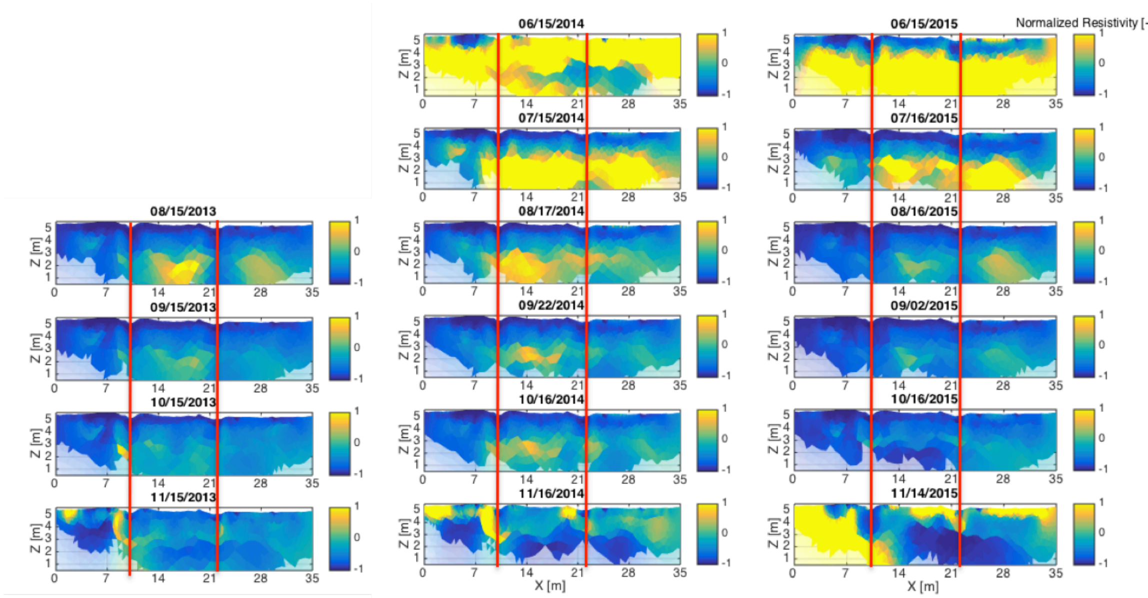

Figure 4: Comparison of temporally-normalized electrical resistivity at different times from August to November of 2013 and from June to November of 2014 and 2015. Red lines separate the HCP (left), FCP (middle) and LCP (right). The normalization was based on the temporal mean of soil electrical resistivity over the 2013-2015 period.

3.2. Estimation of thaw layer thickness from electrical resistivity data

In this section, we combined the probe-based TLT measurements along the study transect (7 datasets) and co-located soil electrical resistivity from the ERT images to determine the resistivity threshold for separating the thaw layer and permafrost. The reason we used this approach is that the number of probe-based TLT measurements is sparse and insufficient to perform the spatiotemporal analysis of TLT. Meanwhile, ERT measurements collected from 2013 to 2015 are plentiful in space and time. As a result, if TLT can be derived from ERT measurements, we can explore the spatiotemporal variations of TLT with high spatiotemporal resolution over the duration of the ERT autonomous acquisition period.

Due to the lateral heterogeneity of polygon morphology and soil characteristics, a common electrical resistivity threshold for the whole transect is not feasible. Consequently, an individual threshold was defined at each ERT electrode location where the probed-based TLT measurements were available (71 locations). The threshold was estimated by minimizing the objective function, which represents the misfit between the probed-based and ERT-derived TLT and is defined as below:

$$\Phi\left(\rho_{threshold,j}\right) = \sum_{t=1}^{N}\left(ALT_{Meas,j}^{t} - ALT_{ERT,j}^{t}\right)^{2} \qquad (3)$$

in which Φ is the objective function; $ALT_{Meas,j}^{t}$ and $ALT_{ERT,j}^{t}$, respectively, are the measured and ERT-derived TLT at time t and location j. N=7 is the number of probed-based TLT measurements at location j. The grid search algorithm was employed to determine the resistivity threshold at each location j. The grid search algorithm simply divides the parameter search space into grid nodes and calculates the objective function at each node. The optimal solution is found at the node where the objective function is minimal. For constraining the inversion, we assumed that the maximum TLT is 0.7 m. The electrical resistivity threshold that generates a TLT greater than this value will not be considered.

Figure 5a compares the probed-based and ERT-derived TLT at a 1:1 scale. This is the best agreement between two terms that we can obtain by grid search algorithm. The correlation between them is 0.65. Compared to measurements, TLT derived from soil electrical resistivity is overestimated with a bias ratio of 1.11. The differences between the two TLT values is likely mainly due to the ERT and probed-based TLT measurement errors, BERT inversion errors, and differences in measurement time of ERT and probed-based TLT.

The estimated electrical resistivity thresholds show large spatial variations ranging from 130 to 774 Ohm.m along the transect (Figure 5b). In order to compare these spatial variations with that of the soil electrical resistivity, we plotted the average electrical resistivity at the top 0.3 m on 09/22/2014 as an illustration. The figure shows that the spatial variations of the resistivity threshold are similar to those of the electrical resistivity in the topsoil. The comparison between the resistivity threshold and surface elevation also shows that there is a positive correlation between the resistivity threshold and the surface elevation. This can be explained by the fact that soil tends to be drier at higher elevations, and therefore, the soil electrical resistivity is also larger. For example, the threshold is pronounced high at the location *X*=6 m of the HCP because it is situated at the higher elevation than the other locations along the transect.

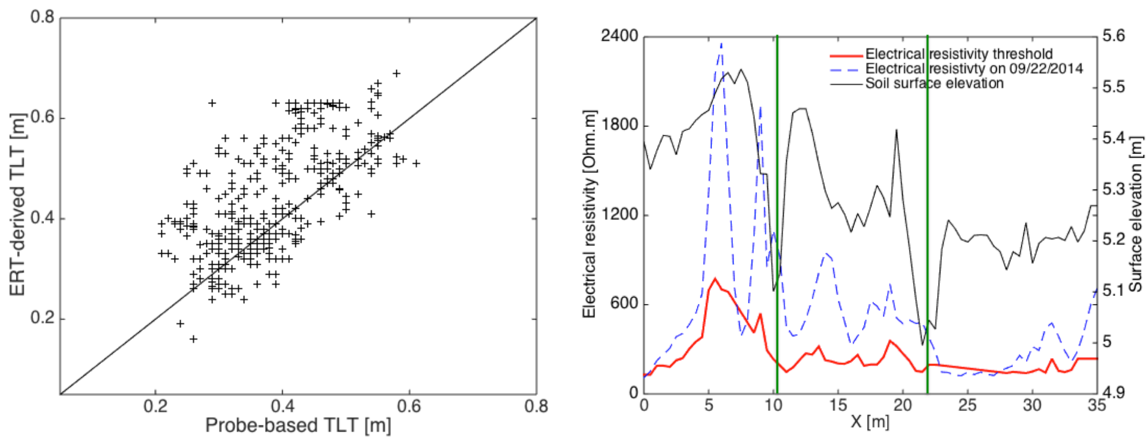

(a) (b)

Figure 5: (a) Comparison of ERT-derived and probed-based TLT. The figure is the best agreement between these two terms obtained by grid search optimization. (b) Electrical resistivity threshold (solid red line), average electrical resistivity at the top 0.3 m on 09/22/2014 (dashed blue line) and surface elevation (solid black line) along the transect. Two solid green lines separate the HCP, FCP and LCP.

3.3. Spatial and temporal variations of thaw layer thickness

Based on the electrical resistivity thresholds determined in the previous section, we estimated TLT along the intensive transect from the soil electrical resistivity images. Figure 6 presents TLT versus time and space for the three years 2013, 2014 and 2015. As for the spatial variations of TLT, the figure indicates that while there is not much difference in TLT between the HCP and FCP, TLT at the LCP is significantly larger than that at the HCP and FCP (except for the HCP location *X*=1 – 6 m). TLT is also different within each polygon type, especially at the HCP. TLT at the HCP location *X*=1-6 m is larger than that at the HCP location *X*=6-10 m. For example, while TLT in 2015 at *X*=1-6 m is up to 0.69 m, that at *X*=6-10 m is less than 0.5 m. In the section 4.2 below, we will prove that while the difference in TLT among the polygon types is caused primarily by the topography morphology, the difference within each polygon is controlled by the soil properties.

As for the temporal variations, Figure 6 also shows that freezing occurs later at the LCP than at the HCP and FCP. At the end of growing season, TLT at the LCP is considerably thicker than the FCP and HCP. For example, on 10/31/2013, the average TLT at the LCP is around 0.44 m, it is 0 and 0.05 m at the HCP and FCP, respectively. Thawing at the HCP and FCP also occurs earlier than that at the LCP but the difference is relatively small among these polygon types.

Through comparing TLT over the three years of measurements, we found that the onset of thawing and freezing was different in different years. For example, thawing began much earlier in 2015 (06/24/2015) than in 2014 (07/05/2014) because air temperature in early summer of 2015 is higher than that in 2014. Due to thicker snow depth, freezing in 2013 occurred later than in 2015, which is especially visible at the LCP. While there was no thaw layer on 10/31/2015, TLT on that date was relatively high in 2013 (0.44 m). These relationships between the thaw/freeze onset and meteorological forcing will be subsequently described section 4.4 below.

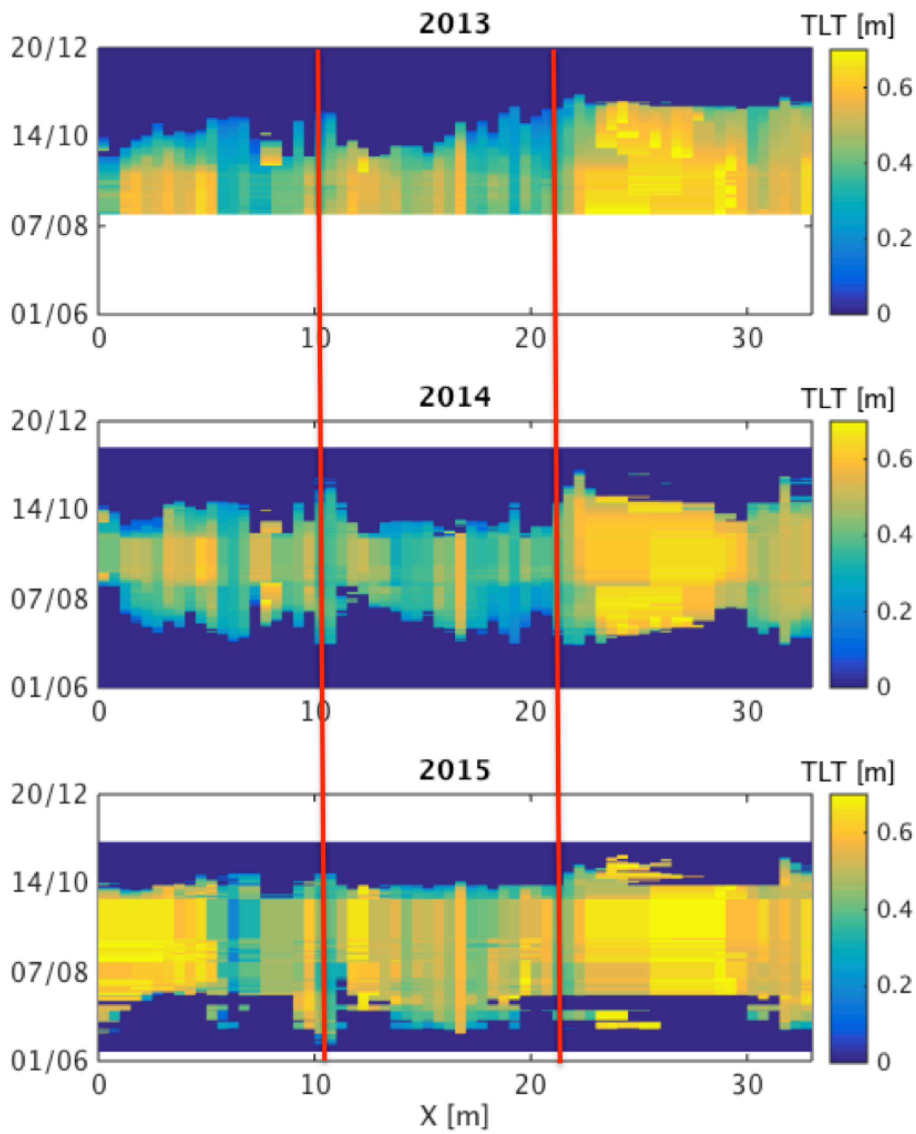

Figure 6: The ERT-derived TLT versus time and space along the ERT transect and over the 2013-2015 period. For comparing the TLT variations of different years, we considered the fixed time period from 01 June to 20 December of each year. White regions represent no data periods. Red lines separate the HCP (left), FCP (middle) and LCP (right).

4. Numerical simulation

4.1. Surface-subsurface hydro-thermal model

In this section, we physically explain the above spatiotemporal variations of electrical resistivity and TLT as well as the factors controlling these variations using numerical simulations. We performed 1-D hydro-thermal simulations in a soil column using CLM model. CLM can simulate hydro-thermal processes from bedrock to the top of canopy with consideration of different land surface processes (e.g., evapotranspiration, radiation balance, snow melting/accumulation) and the phase transition of water (from liquid to ice and vice versa). Soil heat conduction in the subsurface is modeled by the diffusion equation, while soil liquid water dynamics is modeled by Richard's equation (Richards, 1931) with influences of runoff, evaporation, canopy transpiration, root water uptake, and groundwater recharge. Evaporation and transpiration are separately calculated for the soil surface and vegetation using the Monin-Obukhov similarity theory. Melting or freezing occurs when temperature in snow/soil greater or lower than the water freezing temperature (273.15 K). The rate of phase change is determined by the energy excess (for melting) or deficit (for freezing) that needs to change soil/snow temperature to the water freezing temperature. For more information about this model, we refer to Oleson et al. (2013).

In CLM, soil hydro-thermal parameters (i.e., soil thermal conductivity, heat capacity, saturated hydraulic conductivity and water retention curve) are calculated from soil types (sand, clay and soil organic content). Formulas for these relationships are presented in details in Lawrence and Slater (2008). As for vegetation, CLM allows assignment of 17 plant functional types (PFTs) with the predefined leaf area index (LAI), stem area index (SAI), and plant top and bottom heights. In this study, we selected the *C3 Arctic grass* plant type.

We developed a soil column including 32 soil layers in which hydrological simulation was performed at 27 topsoil layers and thermal simulation was performed at all 32 layers. The total thickness of 27 topsoil layers was 2.4 m and that of 5 bottom layers was 3.1 m. We performed CLM simulations over the period from 01/01/2013 to 12/31/2015. The model was run during a spin-up period from 01/01/1996 to 12/31/2012 to generate realistic initial conditions for our simulations. Meteorological input data for CLM includes atmospheric temperature, pressure, precipitation, wind speed, and downward solar and longwave radiation. These data in the 1996-2013 period were obtained from the NGEE database (Xu and Yuan, 2014). For the 2013-2015 period, we obtained precipitation data from Barrow Airport station. The other data were taken from the NOAA Barrow station (http://www.esrl.noaa.gov/gmd/obop/brw/). CLM can provide multiple outputs such as soil temperature and soil liquid/ice content at different depths, runoff, surface water depth, snow depth, evaporation, transpiration, infiltration and groundwater recharge, etc. TLTs are determined as the largest soil depth where soil temperature is greater than or equal to the water freezing temperature.

We performed four synthetic cases to evaluate the influence of topsoil properties (SOC content and soil porosity) (using cases *HCP_lowSOC_topLayer, HCP-thinSOC_topLayer, and HCP_thickSOC_topLayer),* and polygon morphology (using cases *HCP_thinSOC_topLayer and LCP_thinSOC_topLayer)* on the TLT (Table 2). These four cases represent the four typical conditions in term of polygon morphology and soil properties of the LCP and HCP.

Table 2: Description and parameters that were used by CLM model to evaluate the influence of SOC content and polygon morphology on the thaw depth

Case	Parameters	Description
HCP_lowSOC_topLayer	- ***Surface parameters***: *Slope*=$\pi/3$, f_{max}=1 - ***Porosity***: 0-0.125 m: 0.78; 0.125-0.6 m: 0.38; 0.6-5.5 m: 0.5 - ***SOC***: 0-0.125 m: 68%, 0.125-0.6 m: 30%, 0.6-3.1 m: 6%	Relatively low porosity and low SOC content at the top layer (thickness: 0.125 m) of the HCP.
HCP_thinSOC_topLayer	- ***Surface parameters***: *Slope*=$\pi/3$, f_{max}=1 - ***Porosity***: 0-0.075 m: 0.92; 0.075-0.15 m: 0.51; 0.15-0.21 m: 0.66; 0.21-5.5 m: 0.5 - ***SOC***: 0-0.075 m: 96%, 0.075-0.15 m: 16%, 0.15-0.21 m: 44%, 0.21-5.5 m: 6%	High porosity and high SOC content at the thin top layer (thickness: 0.075 m) of the HCP.
HCP_thickSOC_topLayer	- ***Surface parameters***: *Slope*=$\pi/3$, f_{max}=1 - ***Porosity***: 0-0.125 m: 0.92; 0.125-0.15 m: 0.51; 0.15-0.21 m: 0.66; 0.21-3.1 m: 0.5 - ***SOC***: 0-0.125 m: 96%, 0.125-0.15 m: 16%,	High porosity and high SOC content at the thick top layer (thickness: 0.125 m) of

	0.15-0.21 m: 44%, 0.21-5.5: 6%	the HCP.
LCP_thinSOC_topLayer	- ***Surface parameters****: Slope*=0.02, f_{max}=0.2 - ***Porosity***: 0-0.075 m: 0.95; 0.075-0.15 m: 0.82; 0.15-0.21 m: 0.52; 0.21-3.1 m: 0.5 - ***SOC***: 0-0.075 m: 94%, 0.075-0.15 m: 51%, 0.15-0.21 m: 20%, 0.21-5.5: 6 m	High porosity and high SOC content at the thin top layer (thickness: 0.075 m) of the LCP.

4.2. Effect of SOC on the spatiotemporal dynamics of thaw layer thickness

In this section, we explore the impacts of soil porosity and volumetric SOC content on the hydro-thermal dynamics and TLT variations. These impacts were evaluated by comparing the CLM simulation results of three synthetic cases, namely, *HCP_lowSOC_topLayer, HCP_thinSOC_topLayer, and HCP_thickSOC_topLayer* (Table 2 and Figure 7a). The model parameters of these three cases are identical except for the layer thickness, soil porosity and SOC content of the top layer. The *HCP_lowSOC_topLayer* case mimics the soil properties at the HCP-mineral location ~*X*=3 m (see Table 1) with a porosity of 0.78 and a SOC content of 68% at 0-0.125 m depth, and 0.38 and 19% at 0.125-0.6 m depth. The *HCP_thinSOC_topLayer and HCP_thickSOC_topLayer* cases represent the soil properties at the HCP-organic location ~*X*=8 m but with different thicknesses of the top layer to evaluate the effect of the SOC layer thickness on TLT. The top layer thickness is 0.075 m for the *HCP_thinSOC_topLayer* case and 0.125 m for the *HCP_thickSOC_topLayer* case, which are the upper and lower limits of the SOC thickness observed in the ERT transect. For both cases, this top layer has a porosity of 0.92 and a SOC content of 96%.

Figure 7d clearly indicates that when the SOC content at the topsoil layer increases, TLT decreases. TLT also decreases when the thickness of topsoil SOC content increases. Similarly, the soil temperature in the *HCP_lowSOC_topLayer* case is higher than that at the *HCP_thinSOC_topLayer* and *HCP_thickSOC_topLayer* cases (Figure 7c). However, soil liquid water saturation in the *HCP_lowSOC_topLayer* case is smaller (Figure 7b). This is reasonable because when the SOC content is higher, the soil heat capacity increases and the soil thermal conductivity decreases (Lawrence and Slater, 2008). This causes the summer variations in the atmospheric temperature to propagate more slowly to the deep layers. As a result, the soil temperature is higher and TLT is thicker in *HCP_lowSOC_topLayer* case. In addition, because the organic material holds water better than mineral, the water saturation in the *HCP_thinSOC_topLayer* and *HCP_thickSOC_topLayer* cases is higher than that in the *HCP_lowSOC_topLayer* case. It is worth noting that, there are several abrupt changes in TLTs during the 2013-2014 period. It is because TLTs are very sensitive to the change of soil temperature. As a result, a small change in soil temperature can cause significant variations of TLTs. These abrupt variations appear in 2013-2014 because compared to 2015, air temperature in these years varies in a larger range (Figure 7d).

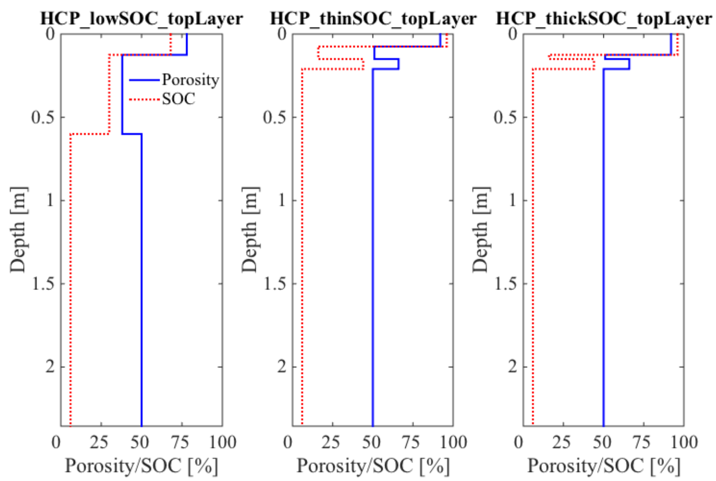

(a) Soil porosity and SOC profiles

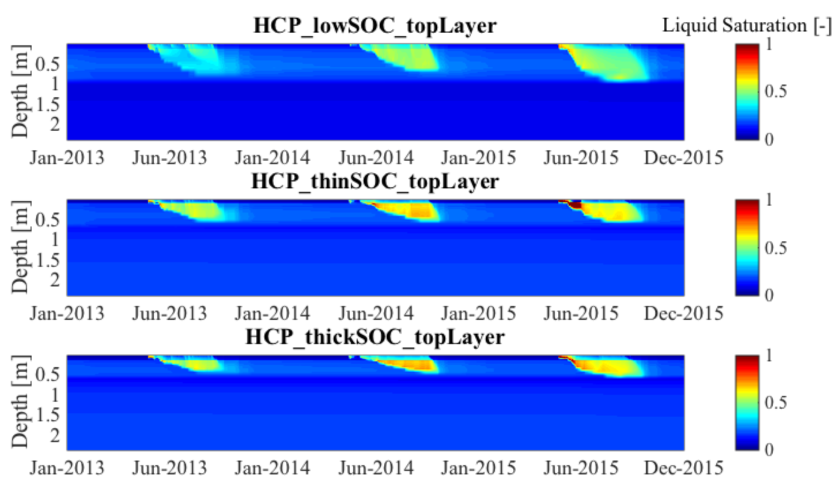

(b) Soil water liquid saturation

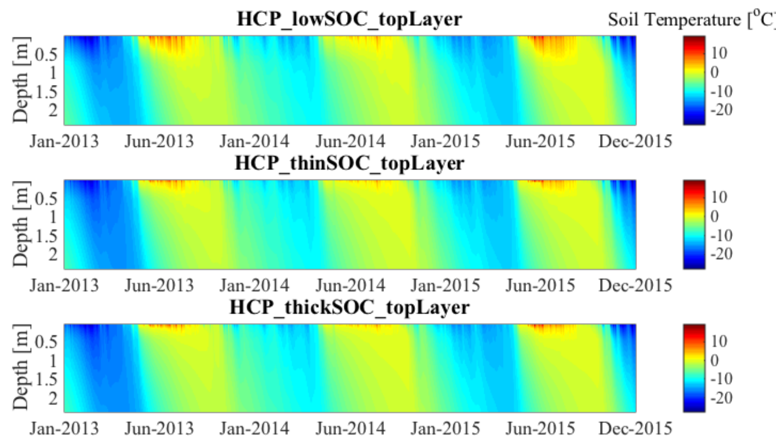

(c) Soil temperature

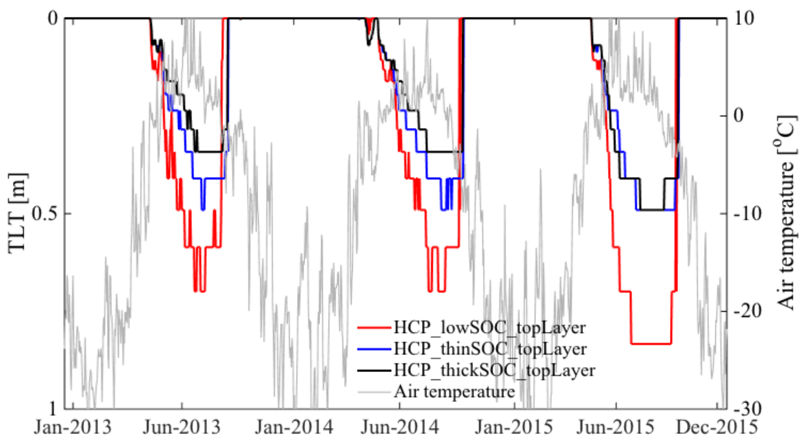

(d) TLT

Figure 7: Soil porosity (solid blue) and SOC (dotted-red) profiles (a). Spatiotemporal variations of soil liquid water saturation (b), soil temperature (c) and TLT (d) in time (*x*-axis) and space (*y*-axis) during 2013-2015 period. For reference, air temperature is also plotted (d). The *HCP_lowSOC_topLayer* case represents the HCP – mineral location with a low SOC content and soil porosity. The *HCP_thinSOC_topLayer and HCP_thickSOC_topLayer* cases mimic the HCP – organic location with a high SOC content and soil porosity at the top layer with a thickness of 0.075 and 0.125 m, respectively.

4.3. Effect of polygon morphology on spatiotemporal variations of thaw layer thickness

In this section, we investigated the impact of polygon morphology on TLT variability by comparing the simulation results of *HCP_thinSOC_topLayer* and *LCP_thinSOC_topLayer* cases. The *LCP_thinSOC_topLayer* case mimics the LCP-SOC location at ~X=29 m (Table 2). Although there are differences in the soil porosity and SOC content, the most profound difference between the two cases is the polygon morphology. Due to the effect of polygon morphology, while a large portion of water from precipitation or/and snowmelt contributes to runoff at the HCP, runoff is much smaller at the LCP. In CLM, the total liquid water at the soil surface is partitioned into surface runoff, surface water storage and infiltration (Appendix A). The surface runoff is calculated by the saturation-excess mechanism, i.e., surface runoff appears only at the saturated parts of soil surface. Runoff is controlled by parameter f_{max} (Equation 2 of Appendix), which is the maximum fraction of soil surface that can be saturated and ranges from 0 to 1. Runoff is potentially larger for a higher f_{max}. The surface water storage represents the wetlands and sub-grid scale water body (e.g., pond). As shown in the Appendix A, the depth of the surface water storage increases when the topographic slope (β) decreases. The decreasing topography slope also causes the smaller lateral drainage of groundwater. In this study, the effect of polygon morphology on the hydro-thermal dynamics was accounted by assigning $f_{max} = 1$, $\beta = \pi/3$ for the *HCP_thinSOC_topLayer* case and $f_{max} = 0.2$, $\beta = 0.02$ for the *LCP_thinSOC_topLayer* case. In addition, at the beginning of the simulation period (01/01/1996), the soil porosity at the LCP was fully filled by liquid water and ice, while ice and liquid water content at the shallow surface of the HCP (≥ 0.4 m) was equal to 20% of the porosity. Below this depth, the soil porosity was also fully saturated.

Figure 8e shows that the TLT at the HCP is shallower than that at the LCP, which is suitable with the observations derived from ERT measurements. The HCP was only relatively wet when melting occurs and then became drier because a large part of liquid water flowed down to its surrounding lower locations. The surface water body appears at the beginning of snowmelt period and rapidly disappears (Figure 8a). By contrast, because runoff was relatively small, soil at the LCP was fully saturated and the surface water storage still exists (Figure 8a, c). Snow depth at the LCP is also higher than at the HCP (Figure 8b). It is because at the beginning of winter, when first snow falls, it may transform to liquid (due to the fact that soil surface temperature is still greater than $0^{o}C$). At the HCP, soil is unsaturated and slope is high, so this liquid mainly partitions into runoff and infiltration. Meanwhile, this liquid remains at the surface of the LCP because soil at the LCP is totally saturated and its slope is low. When soil temperature is equal or below $0^{o}C$, surface water is transformed to ice. The thicker snow layer keeps soil at the LCP warmer during the winter and costs less heat to melt when summer comes, which makes a deeper thaw depth. Within the soil layer, the ice/liquid water content impacts the freezing/thawing in two opposite ways. Higher ice/liquid water content at the LCP leads to the higher soil thermal conductivity, which helps to move more heat from the top to lower layers for thawing. By contrast, higher ice content requires more heat to thaw it. As a result, the competition between these two processes will influence the TLT variations. It is worth noting that in this study we did not consider the difference in vegetation characteristics between the HCP and LCP. Lichens, which primarily cover the HCP, have a higher albedo than graminoid, which mainly cover the LCP. Therefore, inclusion of this spatial variability of vegetation may more increase the difference in TLT between the HCP and LCP. In addition, because CLM is a 1-D model, the influence of the subsurface lateral flow was not accounted for in this study. We also only concentrated on the hydro-thermal dynamics in the active layer and shallow permafrost (top 2.4 m). The dynamics of the saline permafrost layer that is partially unfrozen was not considered.

Figure 8e also shows that both thawing and freezing at the HCP occurs earlier than at the LCP. This can be explained by the fact that the thicker snow layer in winter and the thicker water surface layer in summer at the LCP caused soil at the LCP respond more slowly to the variations of atmospheric temperature. In addition, more ice/liquid water content at the HCP also takes a longer time to melt.

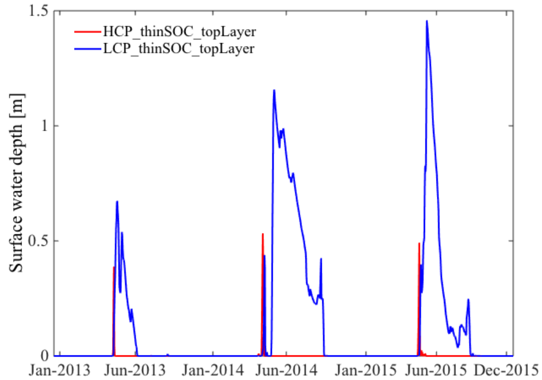

a) Surface water depth

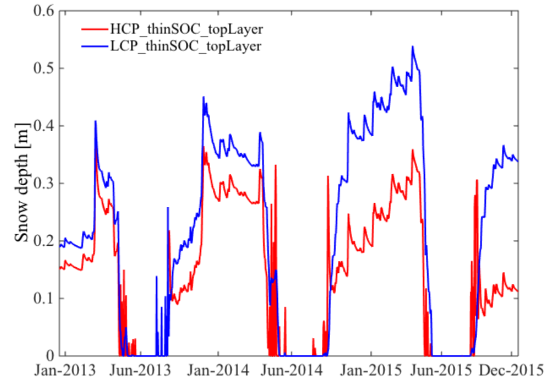

b) Snow depth

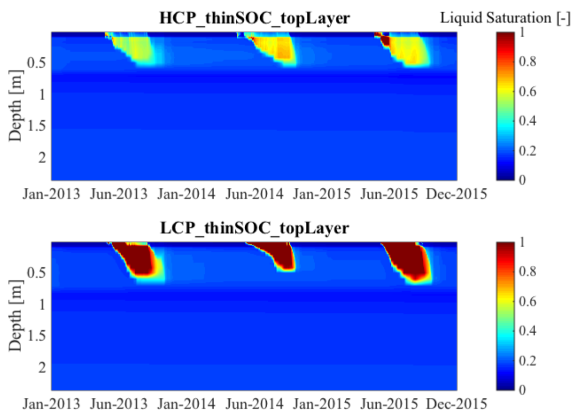

c) Soil liquid water saturation

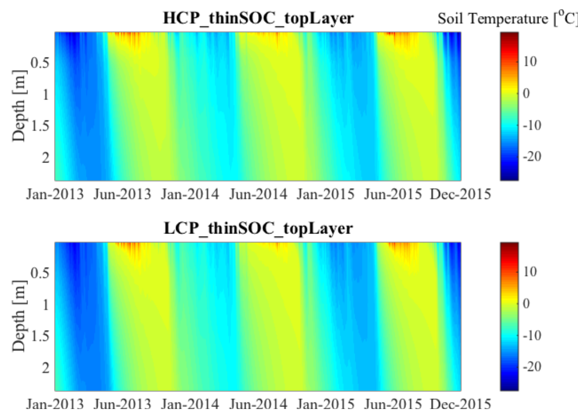

d) Soil temperature

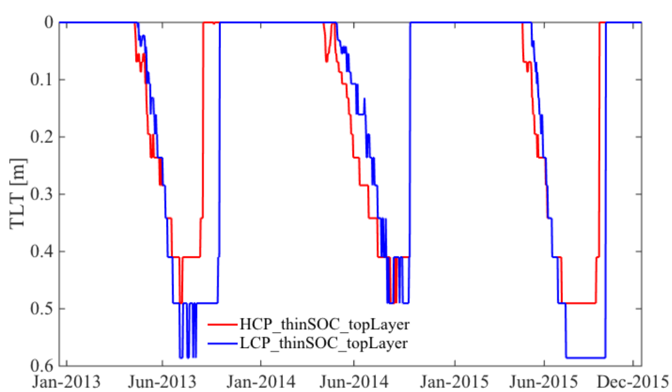

e) TLT

Figure 8: (a, b) Simulated surface water depth and snow depth; (c, d, e) Variations of soil liquid water saturation, soil temperature and TLT in time (*x*-axis) and soil depth (*y*-axis) during 2013-2015 period. The *HCP_thinSOC_topLayer* case represents the HCP with $f_{max} = 1, \beta = \pi/3$, and the *LCP_thinSOC_topLayer* case

represents the LCP with $f_{max} = 0.2$, $\beta = 0.02$.

4.4. Effect of meteorological forcing on temporal dynamics of hydro-thermal variables and TLT

To explore controls on TLT temporal variations, we present in Figure 9 the measured meteorological forcing data (air temperature, yearly-accumulated snow precipitation and rainfall) as well as simulated snow thickness and simulated soil temperature at depths of 0.02, 0.13 and 0.5 m during the 2013-2015 period for the *LCP_thinSOC_topLayer* case. For comparison, soil temperature at a depth of 0.5 m is also presented. In order to evaluate the agreement between modeling and simulation of soil temperature, we employed the Nash-Sutcliffe coefficient (*E*):

$$E = 1 - \frac{\sum_{t=1}^{T}(\boldsymbol{M}_t - \boldsymbol{O}_t)^2}{\sum_{t=1}^{T}(\boldsymbol{O}_t - \bar{O})^2} \qquad (4)$$

in which $\boldsymbol{M}_t$ and $\boldsymbol{O}_t$ are, respectively, the simulated and measured soil temperature at time t. $\bar{O}$ is the average of measured soil temperature over the measurement period T. The Nash-Sutcliffe coefficient varies from $-\infty$ to 1. The accuracy of model prediction increases when this coefficient approaches 1. Figure 9a shows that the agreement between the CLM simulations and measurements of soil temperature is relatively good with a Nash–Sutcliffe coefficient of 0.86. CLM accurately predicts the soil temperature in summer time of all three years. However, the simulated soil temperature is remarkably lower than the measured value at the beginning of winter. These may come from the fact that the soil freezing temperature at the site is lower than the freshwater freezing temperature due to its salinity while its variations with soil salinity were not accounted for in CLM.

Figure 9c indicates that the simulated TLT is slightly smaller than the ERT-derived TLT and well agrees with probe measurements. This difference may be caused by the overestimation of ERT measurements (see Figure 5a). In addition, in this study we did not try to calibrate the CLM model but used the measured soil properties to directly parameterize the model. As a result, the errors in model prediction may be caused by uncertainties in some model parameters, such as soil porosity, SOC content and topographic factors. Because TLT is very sensitive to the freezing temperature, a small error in soil temperature around the water freezing temperature can cause a significant change in TLT.

As for the temporal variation, Figure 9 indicates that the annual variations in atmospheric temperature (at 2-m above the soil surface) and precipitation (both snow and rainfall) are the primary controls on the temporal variations of TLT. Indeed, comparing to 2014, the atmospheric temperature in summer 2013 and summer 2015 were relatively high (Figure 9a). The maximum air temperature for 2013, 2014 and 2015 is, respectively, 11.6, 10.6 and 12.1 ^{o}C and the average temperature in the summer (from June 15 to September 15) of these three years is 3.8, 3.1 and 3.8 ^{o}C. As a result, the soil temperature in 2013 and 2015 was slightly higher. The time span that TLT exists in 2013 and 2015 is also longer than that in 2014. Comparison of TLT in two years 2013 and 2015 indicates that the time span that TLT remains at its maximum depth (0.6 m) in 2013 was shorter than that in 2015. Although air temperature in the two years was similar, we interpret this difference to be due to the presence of a thick snow layer (which was caused by large precipitation in the 2014-2015 winter). The snow layer kept the soil warmer, and therefore, was more susceptible to thaw. As for the freezing time, the high precipitation and high air temperature in the 2013 led to the latest freeze onset out of the three years. By contrast, freezing occurred earlier in 2014 due to low air temperature and in 2015 due to thin snow depth.

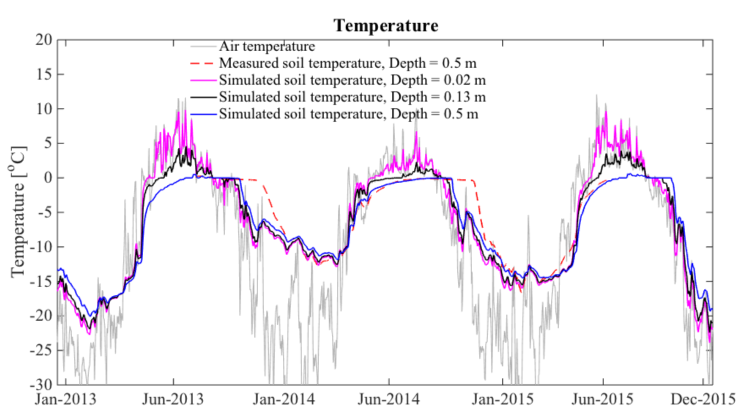

(a) Measured air temperature at 2 m above the soil surface, measured soil temperature at 0.5 m depth and simulated soil temperature at 0.02, 0.13 and 0.5 m

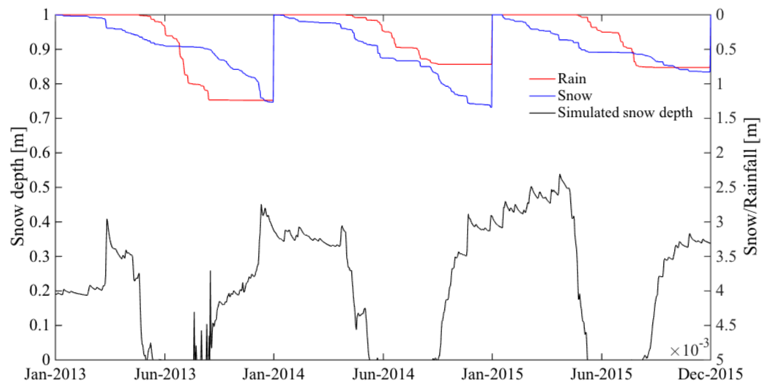

(b) Measured Yearly-accumulated snow/rainfall precipitation and simulated snow depth

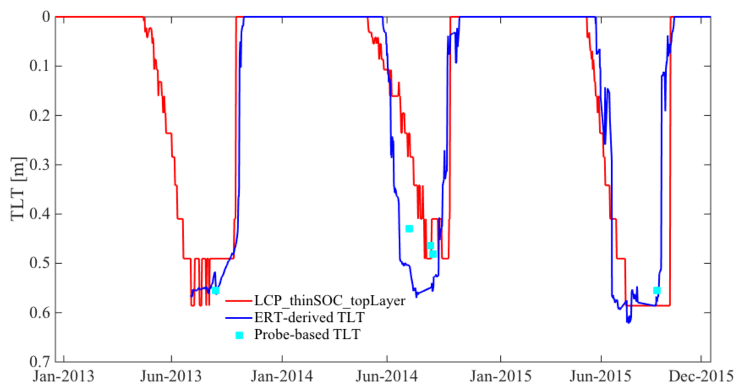

(c) Simulated and ERT-derived TLT

Figure 9: (a) Observed atmospheric temperature at 2-m above the soil surface, measured soil temperature at 0.5 m depth and simulated soil temperature at depths of 0.02, 0.13 and 0.5 m during 2013-2015; (b) Observed yearly-accumulated snow and rainfall precipitation and simulated snow thickness; (c) Simulated, ERT-derived and probe-based TLT in the same 3-year period. Soil temperature, snow thickness, and TLT were obtained by CLM simulation with the *LCP_thinSOC_topLayer* case. Atmospheric temperature and snow/rainfall precipitation were measured at the Barrow site. Measured soil temperature at a depth of 0.5 m from 08/15/2013 to 08/07/2015 was obtained at the LCP of the intensive ERT transect.

5. Conclusion

This study analyzes the spatiotemporal dynamics of the electrical resistivity and TLT along a 35-m intensive transect in Barrow, AK by jointly using ERT measurements and through performing physically-based modeling simulations. The spatiotemporally dense ERT measurements allowed investigation of the annual variations of electrical resistivity and TLT as well as their comparisons in different years and seasons. By combining measurements and numerical simulations, our research provides a valuable approach to confidently interpret the spatiotemporal variations of TLT. The numerical simulation supports our ERT based interpretation of TLT spatial variability and dynamics, while the measurements enhanced the reliability of the numerical modeling, providing validations of simulation results and insights about sources of errors.

Based on the probe-based TLT measurements and co-located soil electrical resistivity images obtained by inversion of ERT data, we estimated the electrical resistivity thresholds along the intensive transect that separated the thaw layer from permafrost. The electrical resistivity thresholds were estimated by minimizing the misfit between point TLT measurements and those obtained from ERT using the grid search algorithm. Using these thresholds, we then derived TLT from electrical resistivity images in the 2013-2015 period. We subsequently analyzed the spatiotemporal variations of both soil electrical resistivity and ERT-derived TLT. The spatial analysis indicates that within each polygon feature, TLT at locations with high SOC content is thinner than locations with low SOC content values. Compared to the LCP, the HCP is drier and has a shallower thaw layer. The freezing occurred earlier at the HCP than at the LCP. The temporal analysis shows that of three years 2013, 2014, and 2015, TLT in 2014 is smallest. Using this approach, we were able to determine TLT with a high spatiotemporal resolution over a long period. This in turn allowed to investigate the TLT dynamics in detail, which had not been possible in previous studies. However, uncertainties of TLT values obtained by this approach were not quantitatively considered in this study. The main uncertainty sources include measurement errors of ERT and thaw probe, ERT inversion uncertainties and resistivity threshold uncertainties. Our on-going study will individually quantify each of these uncertainties and their contribution to the uncertainties of ERT-derived TLTs.

The numerical simulations were performed to identify the factors that control the spatiotemporal variations of TLT and electrical resistivity. We investigated the influence of soil properties, polygon morphology and meteorological forcing on the spatiotemporal dynamics of the soil electrical resistivity and TLT. The results show that the spatial variations of TLT within each polygon feature are due to the soil porosity and SOC content. At the locations with a higher SOC content and correlated soil porosity, the soil thermal diffusivity is lower, and therefore, the heat flux from the top to lower layers in the summer is smaller. As a result, TLT at these locations is shallower. Meanwhile, the difference in TLT among the polygon features HCP, FCP and LCP strongly depends on polygon morphology. At the LCP, the snow layer is thicker due to the phase transition of surface water to ice and the entrapment of snow. The isolation effect of this thicker snow layer causes the thawing and freezing at the LCP occur later than those in the HCP, and makes the maximum TLT larger at the LCP. The temporal variations of TLT are strongly controlled by the atmospheric temperature and precipitation. TLT in 2014 is thinnest because the atmospheric temperature in summer of this year is low. Due to thick snow layer, which was caused by large precipitation, the freezing in 2013 occurred later than the other two years. TLT in 2015 was largest due to the fact that the summer temperature was high and the snow in the 2014-2015 winter was thick. Our conclusion about the role of SOC content is similar to Atchley et al. (2016), who investigated the individual impact of SOC, liquid water saturation, surface water in summer, and snow depth in winter. However, because snow depth, surface water, liquid water saturation in Barrow are closely related and controlled by polygon morphology, we evaluated the impact of polygon morphology on snow depth, surface water and liquid saturation and their overall contribution to TLT, rather than assessing each of these topography-controlled factors individually as per Atchley et al (2016).

By comparing TLT derived from probe and ERT measurements and CLM simulation results, we found that the CLM model estimated the spatiotemporal variations of TLT well and could be used to identify the factors controlling these variations. However, there are still some limitations of this model. First, the freezing temperature is fixed in CLM so that it cannot account for the impact of soil salinity on freezing/thawing. Secondly, CLM only considers the diffusive heat transport and ignores the advective heat transport. As a result, the heat exchange between the top and lower layers simulated in the model is smaller than the reality, especially at the HCP where soil water dynamics is stronger than at the LCP. Thirdly, the subsurface lateral flows of heat and water were not simulated in CLM, which may influence the evaluation of topography effect. Finally, the dynamics of heat and liquid water in the saline permafrost layer were not considered in this study due to lack of information of soil properties at this layer.

This study demonstrates that combination of the above and below-ground measurements with the numerical modeling can help us to better understand the TLT dynamics and controls on their spatial and temporal variations. It provides important knowledge about the relationship between TLT and polygon morphology, soil properties and atmospheric forcing for upscaling from local scale with intensive dense measurements to larger scales, which is crucial for assessing the permafrost feedbacks to global warming.

Acknowledgements. The Next-Generation Ecosystem Experiments (NGEE Arctic) project is supported by the Office of Biological and Environmental Research in the DOE Office of Science. This NGEE Arctic research is supported through contract number DE-AC02-05CH11231 to Lawrence Berkeley National Laboratory. The authors would like to thank NGEE Arctic PI StanWullschleger (ORNL) for support and Thomas Günther for providing the BERT codes.

References

1. Archie, G. E.: The electrical resistivity log as an aid in determining some reservoir characteristics, Society of Petroleum Engineers, T. AIME, 146, 54–62, 1942.
2. Arcone, S. A., Lawson, D. E., Delaney, A. J., Strasser, J. C., & Strasser, J. D. (1998). Ground-penetratinng radar reflection profiling of groundwater and bedrock in an area of discontinuous permafrost. Geophysics, 63(5), 1573-1584.

3. Atchley, A. L., Coon, E. T., Painter, S. L., Harp, D. R., & Wilson, C. J. (2016). Influences and interactions of inundation, peat, and snow on active layer thickness. Geophysical Research Letters, 43(10), 5116-5123.
4. Blok, D., Heijmans, M. M. P. D., Schaepman-Strub, G., Kononov, A. V., Maximov, T. C., & Berendse, F. (2010). Shrub expansion may reduce summer permafrost thaw in Siberian tundra. Global Change Biology, 16(4), 1296-1305.
5. Briggs, M. A., Campbell, S., Nolan, J., Walvoord, M. A., Ntarlagiannis, D., Day-Lewis, F. D., & Lane, J. W. (2017). Surface geophysical methods for characterising frozen ground in transitional permafrost landscapes. *Permafrost and Periglacial Processes*, *28*(1), 52-65.
6. Brown, J., Hinkel, K. M., & Nelson, F. E. (2000). The circumpolar active layer-monitoring (CALM) program: Research designs and initial results 1. Polar geography, 24(3), 166-258.
7. Chen, A., A. D. Parsekian, K. Schaefer, E. Jafarov, S. Panda, L. Liu, T. Zhang, and H. Zebker (2016), Ground-penetrating radar-derived measurements of active-layer thickness on the landscape scale with sparse calibration at toolik and happy valley, Alaska, Geophysics, 81 (2), H9-H19.
8. Dafflon, B., Hubbard, S., Ulrich, C., Peterson, J., Wu, Y., Wainwright, H., & Kneafsey, T. J. (2016). Geophysical estimation of shallow permafrost distribution and properties in an ice-wedge polygon-dominated Arctic tundra region. *Geophysics*, 81(1), WA247-WA263. doi: 10.1190/geo2015-0175.1
9. Dafflon, B., R. Oktem, J. Peterson, C. Ulrich, A.P. Tran, V. Romanovsky & S. Hubbard (2017). Coincident aboveground and belowground autonomous monitoring to quantify covariability in permafrost, soil, and vegetation properties in Arctic tundra. Journal of Geophysical Research – Biogeosciences, 122, 1321–1342, doi:10.1002/2016JG003724.
10. Jørgensen, A. S., & Andreasen, F. (2007). Mapping of permafrost surface using ground-penetrating radar at Kangerlussuaq Airport, western Greenland. Cold regions science and technology, 48(1), 64-72.
11. Hilbich, C., C. Hauck, M. Hoelzle, M. Scherler, L. Schudel, I. Völksch, D. Vonder Mühll, and R. Mäusbacher (2008). Monitoring mountain permafrost evolution using

electrical resistivity tomography: A 7-year study of seasonal, annual, and long-term variations at Schilthorn, Swiss Alps. Journal of Geophysical Research: Earth Surface, 113(F1).

12. Hinkel, K. M., Doolittle, J. A., Bockheim, J. G., Nelson, F. E., Paetzold, R., Kimble, J. M., & Travis, R. (2001). Detection of subsurface permafrost features with ground-penetrating radar, Barrow, Alaska. Permafrost and Periglacial Processes, 12(2), 179-190.
13. Hinkel, K. M., and F. E. Nelson (2003), Spatial and temporal patterns of active layer thickness at Circumpolar Active Layer Monitoring (CALM) sites in northern Alaska, 1995–2000, J. Geophys. Res., 108, 8168, doi:10.1029/2001JD000927, D2.
14. Hinzman, L.D., Kane, D.L., Gieck, R.E. and Everett, K.R., 1991. Hydrologic and thermal properties of the active layer in the Alaskan Arctic. Cold Regions Science and Technology, 19(2), 95-110. doi:10.1016/0165-232X(91)90001-W
15. Hinzman, L.D., Bettez, N.D., Bolton, W.R., Chapin, F.S., Dyurgerov, M.B., Fastie, C.L., Griffith, B., Hollister, R.D., Hope, A., Huntington, H.P. and Jensen, A.M., 2005. Evidence and implications of recent climate change in northern Alaska and other arctic regions. Climatic Change, 72(3), 251-298.
16. Hubbard, S.S., Gangodagamage, C., Dafflon, B., Wainwright, H., Peterson, J., Gusmeroli, A., Ulrich, C., Wu, Y., Wilson, C., Rowland, J. and Tweedie, C., 2013. Quantifying and relating land-surface and subsurface variability in permafrost environments using LiDAR and surface geophysical datasets. Hydrogeology Journal, 21(1), 149-169.
17. Kane, D. L., Hinzman, L. D., Gieck, R. E., McNamara, J. P., Youcha, E. K., & Oatley, J. A. (2008). Contrasting extreme runoff events in areas of continuous permafrost, Arctic Alaska. Hydrology Research, 39(4), 287-298.
18. Lawrence, D. M., & Slater, A. G. (2008). Incorporating organic soil into a global climate model. Climate Dynamics, 30(2-3), 145-160.
19. Léger, E., Dafflon, B., Soom, F., Peterson, J., Ulrich, C., & Hubbard, S. (2017). Quantification of Arctic Soil and Permafrost Properties Using Ground-Penetrating Radar and Electrical Resistivity Tomography Datasets. IEEE Journal of Selected Topics in Applied Earth Observations and Remote Sensing, 10(10), 4348-4359.

20. Liljedahl, A.K., Hinzman, L.D., Harazono, Y., Zona, D., Tweedie, C.E., Hollister, R.D., Engstrom, R., and Oechel, W.C. (2011), Nonlinear controls on evapotranspiration in arctic coastal wetlands, Biogeosciences, 8(11), 3375-3389.
21. McClymont, A. F., M. Hayashi, L. R. Bentley, and B. S. Christensen (2013), Geophysical imaging and thermal modeling of subsurface morphology and thaw evolution of discontinuous permafrost, Journal of Geophysical Research: Earth Surface, 118 (3), 1826-1837.
22. Nelson, F. E., Hinkel, K. M., Shiklomanov, N. I., Mueller, G. R., Miller, L. L., & Walker, D. A. (1998). Active-layer thickness in north central Alaska: Systematic sampling, scale, and spatial autocorrelation. Journal of geophysical research-all series, 103, 28-963.
23. Nicolsky, D. J., Romanovsky, V. E., Alexeev, V. A., & Lawrence, D. M. (2007). Improved modeling of permafrost dynamics in a GCM land-surface scheme. Geophysical Research Letters, 34(8), L08501.
24. Oleson, K. W., Lawrence, D. M., Gordon, B., Bonan, G. B., Drewniak, B., Huang, M., Koven, C. D., Levis, S., Li, F., Riley, J. W., Subin, Z. M., Swenson, S. C., and Thornton, P. E. (2013) Technical description of version 4.5 of the Community Land Model (CLM), NCAR,Technical Note NCAR/TN-503CSTR, 420 pp., https://doi.org/10.5065/D6RR1W7M.
25. Painter, S. L., Moulton, J. D., & Wilson, C. J. (2013). Modeling challenges for predicting hydrologic response to degrading permafrost. Hydrogeology Journal, 1-4.
26. Richards, L.A. (1931). Capillary conduction of liquids through porous mediums. Physics. 1 (5): 318–333
27. Rücker, C., Günther, T., & Spitzer, K. (2006). Three-dimensional modelling and inversion of DC resistivity data incorporating topography – I. Modelling. Geophysical Journal International, 166(2), 495-505.
28. Schaefer, K., Liu, L., Parsekian, A., Jafarov, E., Chen, A., Zhang, T., ... & Schaefer, T. (2015). Remotely sensed active layer thickness (ReSALT) at Barrow, Alaska using interferometric synthetic aperture radar. Remote Sensing, 7(4), 3735-3759.
29. Schuur, E. A., Vogel, J. G., Crummer, K. G., Lee, H., Sickman, J. O., & Osterkamp, T. E. (2009). The effect of permafrost thaw on old carbon release and net carbon

exchange from tundra. Nature, 459(7246), 556-559.

30. Tran, A. P., Dafflon, B., and Hubbard, S. S. (2017). Coupled land surface–subsurface hydrogeophysical inverse modeling to estimate soil organic carbon content and explore associated hydrological and thermal dynamics in the Arctic tundra, The Cryosphere, 11, 2089-2109, https://doi.org/10.5194/tc-11-2089-2017.
31. Turetsky, M. R., Wieder, R. K., & Vitt, D. H. (2002). Boreal peatland C fluxes under varying permafrost regimes. Soil Biology and Biochemistry, 34(7), 907-912.
32. Wainwright, H. M., Liljedahl, A. K., Dafflon, B., Ulrich, C., Peterson, J. E., Gusmeroli, A., & Hubbard, S. S. (2017). Mapping snow depth within a tundra ecosystem using multiscale observations and Bayesian methods. The Cryosphere, 11(2), 857-875.
33. Wright, N., Hayashi, M., & Quinton, W. L. (2009). Spatial and temporal variations in active layer thawing and their implication on runoff generation in peat-covered permafrost terrain. Water Resources Research, 45(5).
34. Xu, .X and Yuan, F. (2014). Meteorological forcing at Barrow AK 1985-2013. Next-Generation Ecosystem Experiments (NGEE) Arctic Project, Oak Ridge National Laboratory, Oak Ridge, Tennessee, U.S.A.
35. You, Y., Yu, Q., Pan, X., Wang, X., & Guo, L. (2013). Application of electrical resistivity tomography in investigating depth of permafrost base and permafrost structure in Tibetan Plateau. Cold Regions Science and Technology, 87, 19-26.

Appendix A

1. Saturation-excess runoff

In CLM, the total liquid water at the soil surface ($q_{liq,0}$) is the sum of rainfall arriving at soil surface and snowmelt water. This total liquid water is partitioned into surface runoff, surface water storage and infiltration. The determination of surface runoff (q_{over}) is based on the saturation-excess mechanism, i.e., the runoff occurs at the saturated parts of soil and is calculated as below:

$$q_{over} = f_{sat} q_{liq,0} \quad (1)$$

where $q_{liq,0}$ is calculated as the sum of the precipitation liquid arriving the soil surface and water liquid from snowmelt; f_{sat} denotes the saturated fraction which is calculated as:

$$f_{sat} = f_{max} e^{-0.5 f_{over} z_{\nabla}} \quad (2)$$

in which f_{max}, ranging from 0 to 1, is the maximum saturated fraction; f_{over} is a decay factor (m^{-1}); z_{∇} is the water table depth. In this study, the center of the LCP has a lower elevation compared to surrounding locations. Incoming water from precipitation or/and snowmelt will fill this center pond before generating runoff. In order to simulate this phenomenon, we set f_{max} at a small value (f_{max} = 0.2) to keep water at the surface of the center of LCP.

2. Surface water storage

CLM also considers the water that stays in the depression of the soil surface (surface water storage). The relationship between surface water mass and surface water depth in CLM is formulated as below:

$$W = \frac{d}{2}\left[1 + erf\left(\frac{d}{\sigma\sqrt{2}}\right)\right] + \frac{\sigma}{\sqrt{2\pi}} e^{\frac{-d^2}{2\sigma^2}} \quad (3)$$

Where $erf = \frac{1}{\sqrt{\pi}}\int_{-x}^{x} e^{-t^2} dt$ is the error function; *W* is the surface water storage (kg/m^2); *d* is the surface water depth (m); σ is the microtopography factor and calculated as:

$$\sigma = (\beta + \beta_0)^{\eta} \quad (4)$$

in which $\beta_0 = (\sigma_{max})^{\frac{1}{\eta}}$ with $\sigma_{max} = 0.4$ is the maximum value of σ and $\eta = -3$ is an empirical coefficient.